Engineering Applications of Computational Fluid Mechanics Vol. 7, No. 4, pp. 496–506 (2013)

ANALYSIS OF INTERFERENCE FACTORS OF AIR TURBINE CASCADES

Andrei Gareev, Buyung Kosasih * and Paul Cooper

School of Mechanical, Materials and Mechatronics Engineering, University of Wollongong, Northfields Avenue, NSW 2522 Australia
** E-Mail: buyung@uow.edu.au* (*Corresponding Author*)

ABSTRACT: This paper reports viscous compressible aerodynamics analysis of two-dimensional cascades (arrays of aerofoils). The study elucidates the effect of cascade parameters such as solidity, σ, and angle of attack, α, on the interference between blades. Understanding the interference behaviour is important in the performance analysis of air turbines such as Wells turbine commonly used in oscillating water column (OWC) - wave energy converter (WEC) system. The present analysis shows that isolated two-dimensional lift coefficient modified by interference factors, k_o, based on inviscid flow theory is acceptable for low solidity cascades, i.e. $\sigma \leq 0.5$, and that stall occurs at lower angle of attack in cascade compared to isolated aerofoil. When $\sigma > 0.5$, k_o is shown to depend on both α and σ especially in the post-stall flow. The result suggests that interference factors that is applicable for wide range of flow conditions as in Wells turbines should also include the α effect in the modifier.

Keywords: aerofoils, cascade, computational fluid dynamics, interference factor, solidity, Wells turbine

1. INTRODUCTION

Wide variety of technologies have been proposed to extract energy from ocean waves ranging from floating structures that flex and recover energy through hydraulic systems such as the Pelamis wave farm located off the coast of Portugal (Pelamis, 2012) through to various types of buoy tethered to ocean floor such as the OPT's PowerBuoy (Ocean Power Technologies, 2012). Oscillating Water Column (OWC) system shown in Fig. 1a is one of the most promising wave energy technologies. Full scale examples of such devices are the Limpet on the Isle of Islay in the UK (Whittaker et al., 2003), and the Pico plant in the Azores (Brito-Melo et al., 2008).

Most oscillating water column wave energy converters (OWC-WECs) use axial flow turbines (Fig. 1b) to harness the energy of the oscillating variable velocity air as the free-surface of the water rises and falls inside the OWC chamber. Because of these conditions, the turbines must be capable of effectively harnessing the pneumatic energy generated over a wide range of angles of attack. In the first-level design analysis of OWC-WEC turbines, such as Wells turbine (Figs. 1b and c), the work done by the fluid on the blades is calculated (Gato and Falcao, 1984) in a way similar to BEM approach. Despite of the relative simplicity of the approach, it relies on accurate lift and drag data. Because the flow between adjacent blades in cylindrical or linear series of blades (cascade) can be quite different to that over isolated aerofoils, the cascade lift and drag are different to those of isolated aerofoil due to the "interference" that each blade has on the flow field around its neighbours. For OWC-WEC Wells turbines, which often have high solidity rotors, the interference effect between the blades in circular cascade can be even more significant. The parameters affecting the degree of the mutual interference shown in Fig. 2 include (Weinig, 1964): the solidity of the cascade, σ (= c/s), angle of attack, α, and the blade stagger angle, γ.

The effect of the interference between blades in a cascade is usually expressed in terms of an *interference factor*, k_o, which is the ratio of the lift coefficient of a blade in a cascade, C_L, to that of an isolated blade, C_{L0}. The interference of adjacent blades at various stagger angles has been analytically calculated using inviscid potential flow analysis such as the Weinig's model of linear cascade of flat or curved plates (Weinig, 1964) and aerofoil surfaces as singularities (Raghunathan, 1995 and 1996). These results are expected to be valid in the stall free flow condition.

Weinig's formula has been used by several researchers (Gato and Falcao, 1988 and 1984; Raghunathan and Beattie, 1996) in OWC-WEC turbines analyses. This is acceptable if the turbine operates in stall free conditions. However Wells turbine is well known to have very narrow high efficiency operating condition which can be

Received: 23 Nov. 2012; Revised: 12 Jul. 2013; Accepted: 5 Aug. 2013

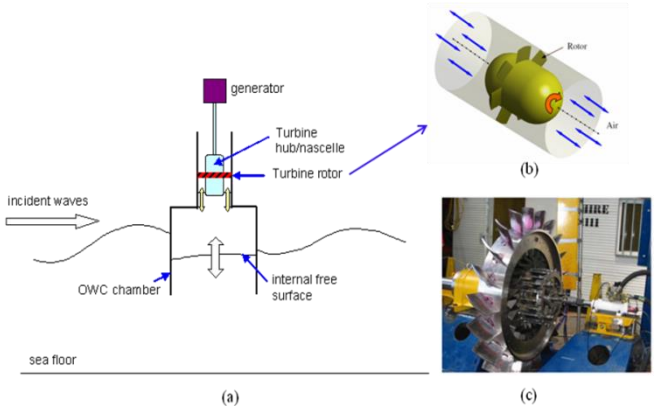

Fig. 1 Schematics of: (a) Oscillating Water Column (OWC) Wave Energy Conversion (WEC) device; (b) Wells turbine and (c) full-scale Denniss-Auld turbine with variable pitch angle blades (Alcorn and Finnigan, 2004).

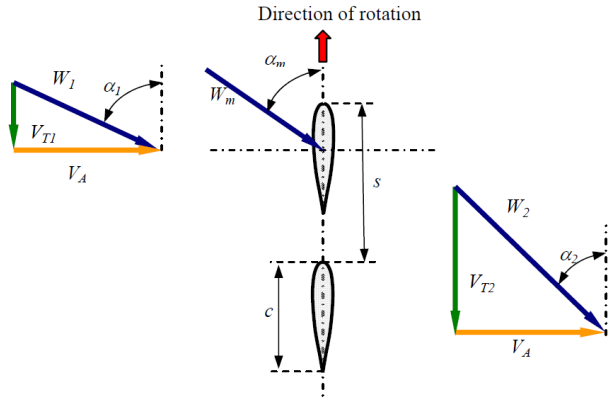

Fig. 2 Cascade on axial flow turbine rotor with stagger angle, $\gamma = 0°$; chord length, c; blade pitch, s; axial air velocity, V_A; and tangential velocity relative to aerofoils, V_T. The angle of attack and relative velocity are defined as $\alpha_m = (\alpha_1 + \alpha_2)/2$ and $W_m = (W_1+W_2)/2$.

attributed to the operation of the turbines under deep stall condition over significant portion of the blades span. Deep stall starting from the tip moving toward mid-span reduces the power output significantly (Torresi et al., 2009). This shows that the use of simple interference factor based on inviscid and infinitesimally thin foils is not suitable for Wells turbine analysis.

A number of approaches to reduce the loss and increase cascade performance have been reported. Sun et al. (2012) demonstrated the effect blade leading profiles and wedge angle on turbine cascades performance. Strong effect was shown on the boundary layer separation and the trailing loss. Constant chord Wells turbine is shown to stall early compared to variable chord turbine resulting in greater efficiency of variable chord turbine by up to 60% (Govardhan and Chauhan, 2007). Guide vanes have also been introduced to increase the tangential velocity at the rotor inlet aiming at increasing turbine efficiency. Kumar and Govardhan (2010) further studied the effect of placing passive fence to reduce the secondary flow losses.

The paper presents the results of CFD analyses of the aerodynamics of linear cascades and discusses the flow field through such cascades particularly the effect of cascade parameters on the incipient of stall and its implication on the blade lift and drag. The merits and inadequacies of the previous inviscid model of axial flow air turbines for OWC-WECs such as that of Weinig (1964) are also discussed.

2. CASCADE INTERFERENCE FACTOR BASED ON INVISCID ANALYSIS

A simplified illustration of infinite linear cascade with staggered blades is shown in Fig. 2. Because of the blades interaction with each other, the lift coefficient, C_L, and the drag coefficient, C_D, are different to that of isolated aerofoil. Modifiers expressed in terms of the ratio of the cascade lift coefficient, C_L, to that of isolated blade, C_{L0}, taken at the same angle of attack, known as the *interference factor* ($k_o = C_L/C_{L0}$) are commonly adopted in Wells turbine analysis. Few experiments to determine k_o have been reported. Raghunathan (1988) carried out experiment with limited range of solidity and in free stall condition, where it is shown that the Weinig's model is still applicable. As consequence, many Wells turbine performance analysis still adopts the interference factor based on linear cascade of infinitesimally thin flat blades (Weinig, 1964). It is expected that at high solidity and high angle of attack the viscous and compressibility effects can lead to different separation mechanism and hence inception of stall. Additionally there is no report on the post-stall aerodynamic behaviour of cascade.

Weinig (1964) showed an exact solution for 2-dimensional potential flow around row of flat plates and the interference factor is independent of attack angle, α, and is only a function of blade stagger angle, γ, and cascade solidity, σ. Using the analytical formulation for the lift coefficient for an isolated aerofoil prior to stall, Weinig (1964) determined the lift coefficient for cascade blade as follows

$$C_L = 2\pi k_o \sin(\alpha_m) \quad (1)$$

where α_m is the angle of attack based on the mean of the flows upstream and downstream of the cascade, and k_o is a complex function of γ and s/c

(or $1/\sigma$) shown in Fig. 3. For the special case with γ = 0°, as in the case of a Wells turbine, the interference factor (Weinig, 1964) is given by

$$k_o = \frac{2s}{\pi c}\tan\left(\frac{\pi c}{2s}\right) \quad (2)$$

Eq. (2) is widely accepted as the lift coefficient modifier or interference factor of fixed-pitch (γ = 0°) Wells turbine blades. C_L modified by Eq. (2) is shown together with experimental data for an isolated NACA0012 aerofoil at Re = 7×10^5 (Sheldahl and Klimas, 1981) in Fig. 4. Solid curve in this figure represents the cascade lift coefficient calculated using the isolated aerofoil data multiplied by the interference factor of Eq. (2). In order to determine k_o, and plot the cascade lift curve, the following cascade dimensions: c = 0.1 m and s = 0.169 m were used in Eq. (2). It can be clearly seen that the lift curve based on the lift data modified by k_o exhibits higher values of C_L than the isolated aerofoil lift coefficient and the deviation seems to start from α_m=10°. On the figure, C_L calculated by CFD compressible model (*) shows reasonable agreement at low angle of attack (5°). However the CFD predicted C_L at stall and post-stall is much greater than the prediction by Eq. (2). It is expected that the cascade interference effect will be significant in the post stall regime. The CFD approach discussed in Section 3 was validated by comparing the coefficient of lift of isolated aerofoil case. The agreement between the experimental curve (dash curve) and the numerical values (o) is very good in the pre-stall region and reasonable in the post-stall region.

Although Eq. (2) has been widely used in the analysis of Wells turbines (Gato and Falcao, 1988; Raghunathan and Beattie, 1996) and compared with experimental measurement of Wells turbine effeiciency (Gato and Falcao, 1988; Raghunathan et al., 1990) to the best of our knowledge, there is still limited validation of the relationship between k_o and σ from practical aerofoil cascades i.e. over large range of angle of attack, and solidity in pre-stall and post stall regimes and hence limited understanding of the cascade effect in post-stall condition.

3. 2-DIMENSIONAL COMPUTATIONAL FLUID DYNAMICS (CFD) MODEL

The present study used ANSYS CFX code to simulate the flows around cascades of relevance to OWC-WEC axial flow turbines under realistic flow conditions i.e. viscous, turbulent flow and

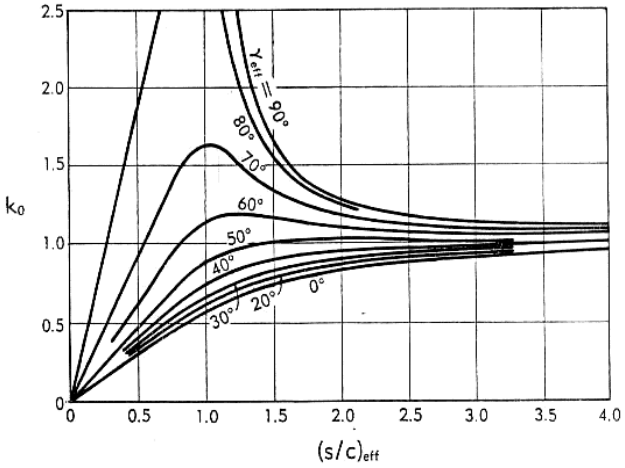

Fig. 3 Interference factor, $k_0 = C_L/C_{L0}$, from potential flow theory (Weinig 1964). γ_{eff} is the stagger angle defined as $\gamma_{eff} = 90° - \gamma$.

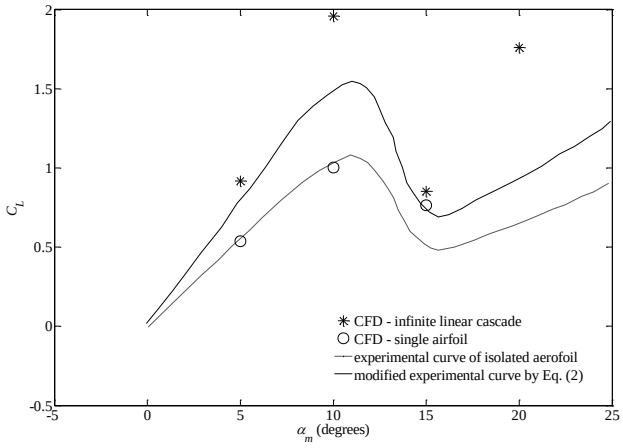

Fig. 4 Comparison of isolated experimental aerofoil lift data C_{L0} by Sheldahl and Klimas (1981) at Re = 7×10^5, corrected cascade lift data C_L (by k_0 for s/c = 1.69, σ = 0.6) and present CFD infinite cascade data.

over practical ranges of angle of attack and Reynolds number. CFD interference factors were derived and presented in terms of the effective angle of attack based on the mean angles between the aerofoil chord, and the upstream and the downstream flow directions, α_m = $(\alpha_1+\alpha_2)/2$, shown in Fig. 2.

2-dimensional, steady and compressible CFD simulations over wide ranges of angles of attack and cascade solidity were carried out. Grid independence was verified for linear cascade simulation and the number of unstructured elements where coefficient of lift remains unchanged with further refinement was of the order of 1.5×10^6 (Gareev, 2011). A typical mesh around the blade and type of boundary conditions used are shown in Fig. 5. *k-ω SST* turbulence model with automatic wall functions and the

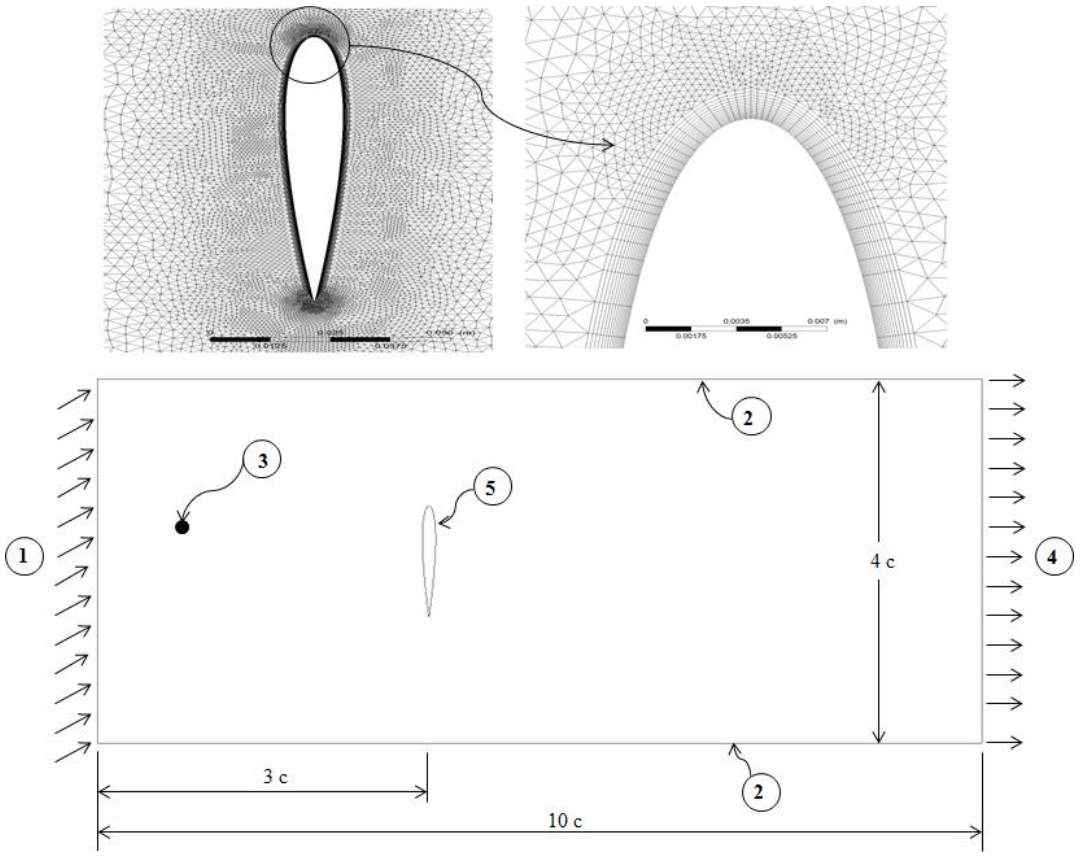

Fig. 5 Typical mesh used in CFD simulations is shown in the upper figures. In general tetrahedral elements were used and prismatic elements defined within inflation layers were used near the aerofoil surfaces. Computational boundary conditions are shown in the lower figure: (1) upstream boundary – specified inlet velocity; (2) upper and lower boundaries - periodic; (3) left and right side boundaries – free-slip wall; (4) downstream boundary – opening with specified static pressure; and (5) airfoil surface – nonslip wall.

"*high resolution*" advection scheme and "*auto timescale*" were used. As the flow can reach high Mach number at the leading edge of the blades where compressibility is significant total energy model to account for the heat transfer was used. The automatic near-wall treatment switches between low-Re near wall formulation when $y^+ < 2$ and otherwise standard wall function formulation to resolve the flow close to the blade surfaces. Inflation layers were used to create fine mesh near the surface resulting in average y^+ between 10 and 20. All simulations were carried out at $Re = 7\times10^5$ (based on chord length).

The computational domain and boundary conditions are shown in Fig. 5. The computational domain was bounded by inlet boundary with specified velocity, turbulent intensity of 5% and air temperature of 20°C. The outlet boundary was specified as opening held at atmospheric static pressure. To model 2-dimensional flow only one cell was used to represent domain thickness. Only one aerofoil was used in the simulation with periodic boundary as the interface between adjacent blades.

4. RESULTS AND DISCUSSIONS

The lift coefficients from the present CFD simulations at $Re = 7\times10^5$ were first compared to experimental isolated aerofoil data (Sheldahl and Klimas, 1981) and to values corresponding to the isolated experimental data modified by Eq. (2) in Fig. 4. It is evident that the CFD predictions are in good agreement with experimental lift data corrected by applying Eq. (2) for $\alpha \leq 10^o$. This confirms the validity range of Eq. (2). However in the post-stall region, the CFD results show significantly higher C_L.

Interference factors for blades chord parallel to the plane of the cascade ($\gamma = 0^o$) cases were analysed for a range of solidities ($1/\sigma = s/c$) and mean angles of incidence, α_m. Results from these simulations are presented in Fig. 6 together with the interference factors calculated using Eq. (2).

It can be seen in Fig. 6 that the interference factors obtained by Eq. (2) (Weinig 1964) and viscous compressible CFD simulations match up to $1/\sigma = 2$ or $\sigma = 0.5$ for all angles of attack up to $\alpha_m = 20^o$. When $\sigma > 0.5$ the viscous and

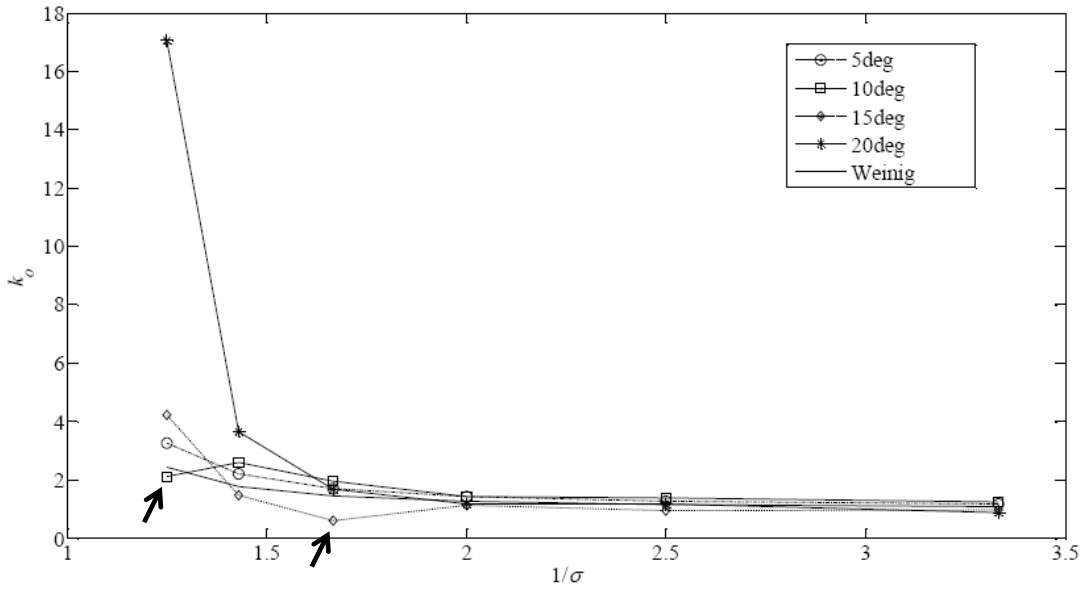

Fig. 6 Lift coefficient interference factors, k_o, for linear cascade ($\gamma = 0$º) of NACA0012 aerofoils as function of $1/\sigma$ and mean angle of incidence, α_m. The solid curve is based on Weinig inviscid flow analysis, Eq. (2). The arrows indicate the stall attack angles at different solidities.

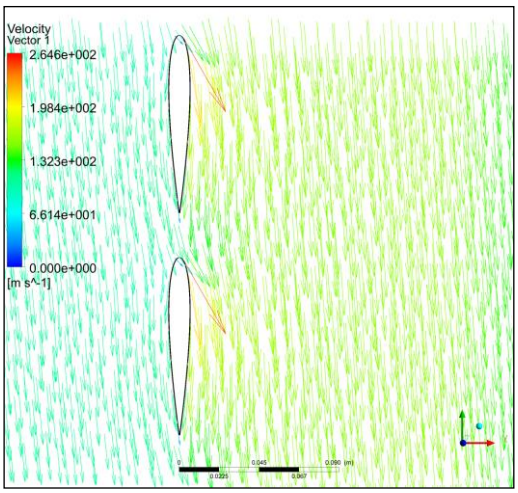

(a) $\alpha_m = 5°$

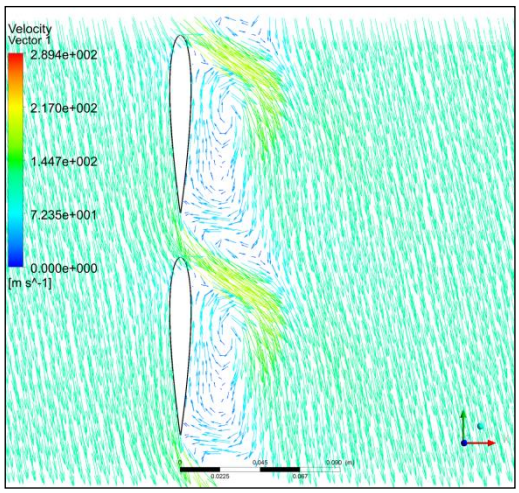

(b) $\alpha_m = 10°$

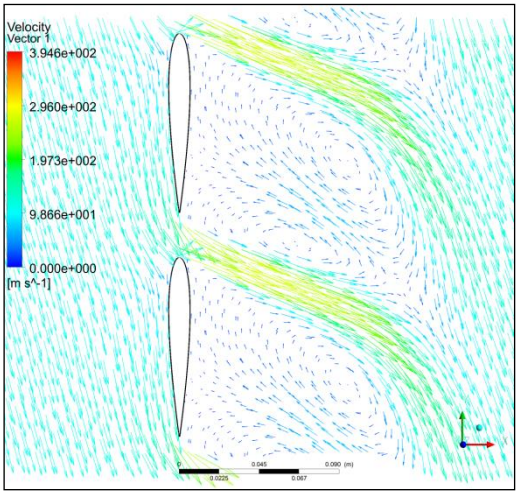

(c) $\alpha_m = 15°$

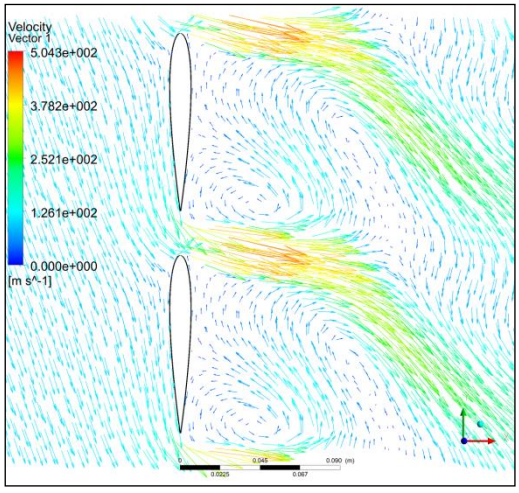

(d) $\alpha_m = 20°$

Fig. 7 Velocity vectors around cascade (NACA0012) of $1/\sigma = 1.25$ ($\sigma = 0.8$) at different mean angles of incidence, α_m.

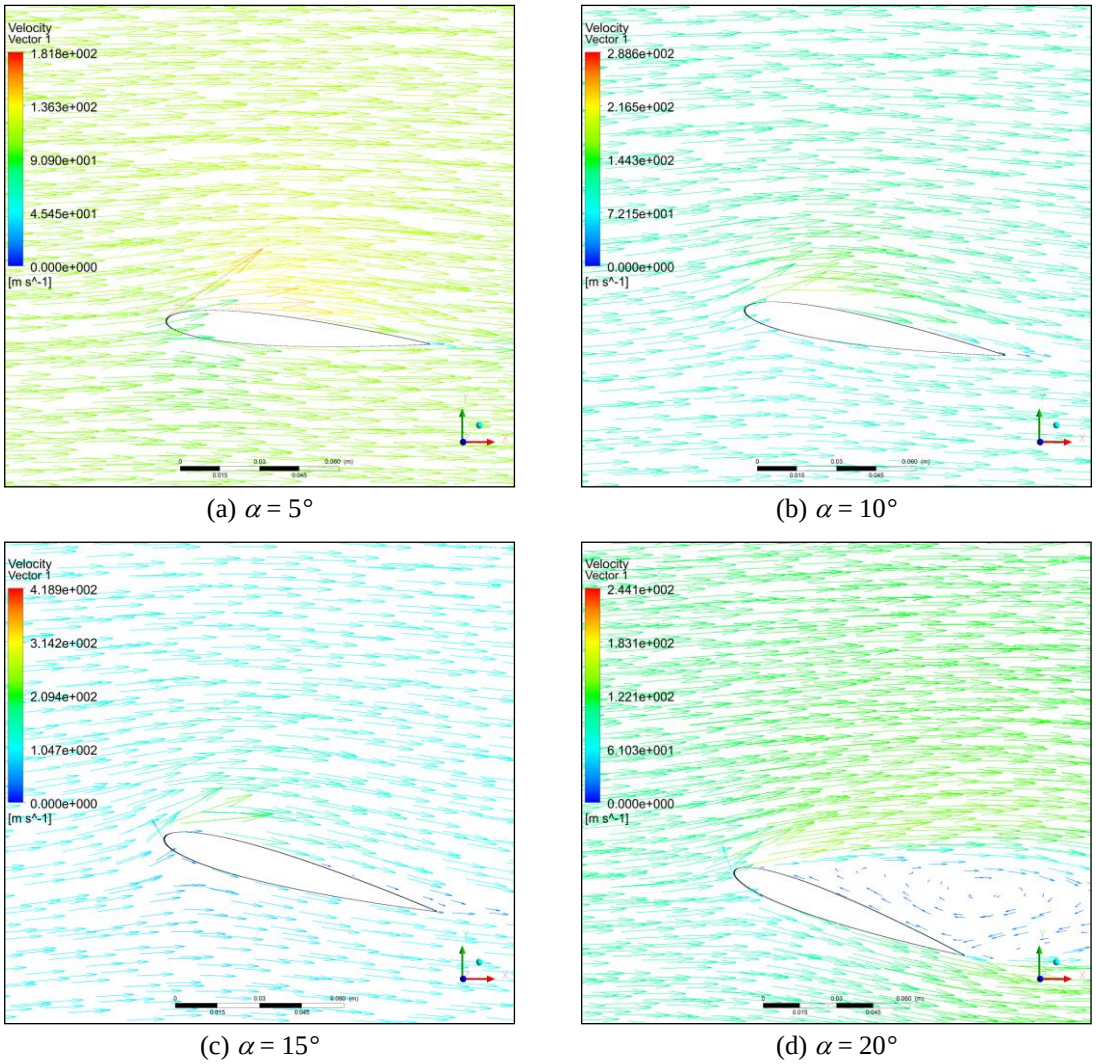

(a) $\alpha = 5°$ (b) $\alpha = 10°$

(c) $\alpha = 15°$ (d) $\alpha = 20°$

Fig. 8 Velocity vectors around isolated aerofoil (NACA0012) at different mean angles of incidence, α.

compressibility effects in general cause greater lift than isolated aerofoil and the effects become more pronounced at high angle of attack. It was found that the difference widens in post-stall region when $\alpha_m > 10^o$.

Figs. 7 and 8 show the velocity vectors around the cascade blades and isolated aerofoil, respectively. It can be seen that in cascade, stall occurs at lower attack angle, namely $\alpha_m = 10^o$ and $\alpha_m = 20^o$ for the isolated aerofoil. The existence of separation bubble over the aerofoil suction side in cascade results in lower lift and hence dip in the interference factor (indicated by arrows in Fig. 7). At $\alpha_m = 10^o$ the flow is already in the post-stall region in contrast to isolated aerofoil where stall is not seen until about 20^o as shown in Fig. 8. This causes the lift to be lower than isolated aerofoil lift. Similar phenomenon is also seen at $\sigma = 0.6$ where cascade stall occurs at $\alpha_m = 15^o$. The drop (indicated by arrows in Fig. 7) in k_o observed at $1/\sigma = 1.25$ ($\sigma = 0.8$) and 1.667 ($\sigma = 0.6$) at $\alpha_m = 10^o$ and 15^o can be explained by the effect of the cascade in lowering stall angle. From this observation it can be concluded that cascade lowers stall angle, the greater the solidity the lower the cascade stall angle.

As the angle of attack increases beyond $\alpha_m > 10^o$, the difference between the Weinig interference factor and the CFD calculated k_o widens. This indicates that cascade effect is more pronounced at high solidity and in post-stall region.

The increase of k_o at high angle of attack ($\alpha_m = 15^o$ and 20^o) seen in Fig. 6 can be attributed to greater pressure difference between the pressure and suction sides of the blades as shown in Figs. 10 and 11. This is not seen when $\alpha_m = 10^o$ in Fig. 9. In fact there is a significant increase in pressure on the suction side (circled in Fig. 9) due to early stall correspond to Fig. 7b, leading to drop in lift.

The effects of cascade solidity on surface pressure distribution are shown in Figs. 9 to 11. Few observations can be made. Increased solidity leads to higher pressure on the pressure sides at $\alpha_m > 10°$ or in the post stall region. At high

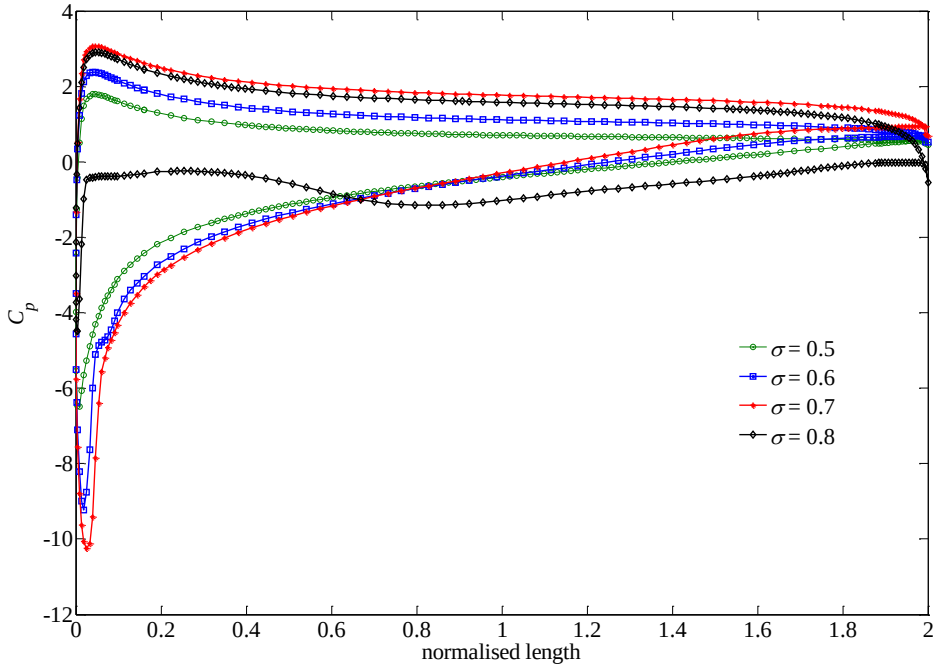

Fig. 9 Surface pressure distributions on cascade blade for different solidities at α_m = 10°. The circle shows high pressure in the separation region when σ = 0.8.

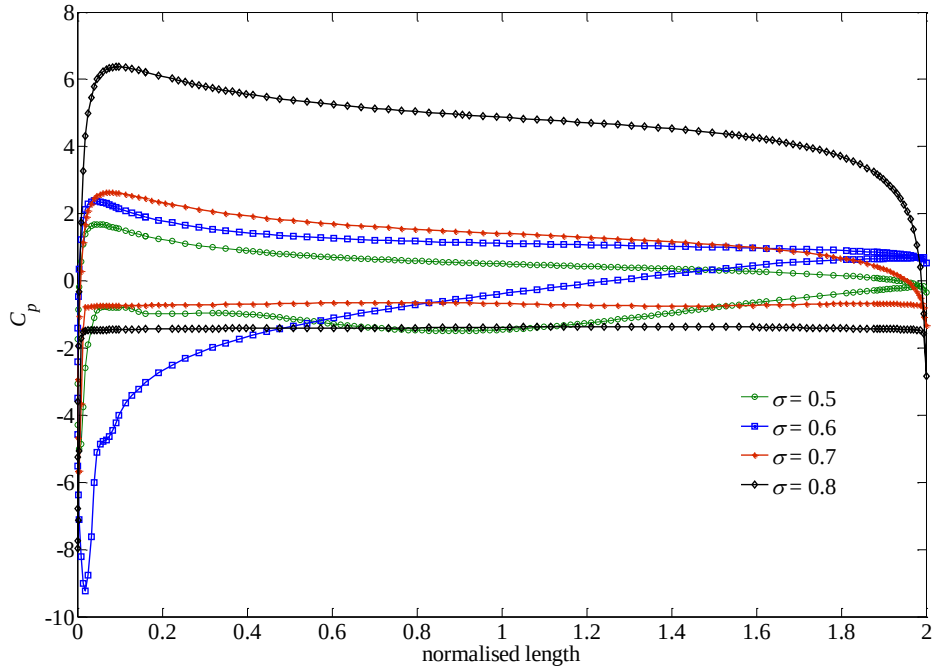

Fig. 10 Surface pressure distributions on cascade blade for different solidities at α_m = 15°.

solidity, $\sigma > 0.7$, pressure distribution on the blade surface is more uniform. It appears that when solidity increases, the proximity of blades induces blockage effect which causes an increase of the surface pressure on the pressure side and decrease of the pressure on the suction side of the cascade (see Figs. 10 and 11), creating larger pressure difference between the suction and the pressure sides. This explains the rapid increases of k_o when $\sigma > 0.7$ ($s/c < 1.42$).

Comparison of the streamlines around isolated aerofoil with that around cascade shows two interesting phenomena. Firstly, as stall is approached with increasing angle of attack the separation zones on the cascade blades start at the leading edges of the blades where in isolated aerofoil the flow remains attached downstream from the leading edge, i.e. until the local adverse pressure gradient causes the flow to detach. Secondly, at higher cascade solidity, the

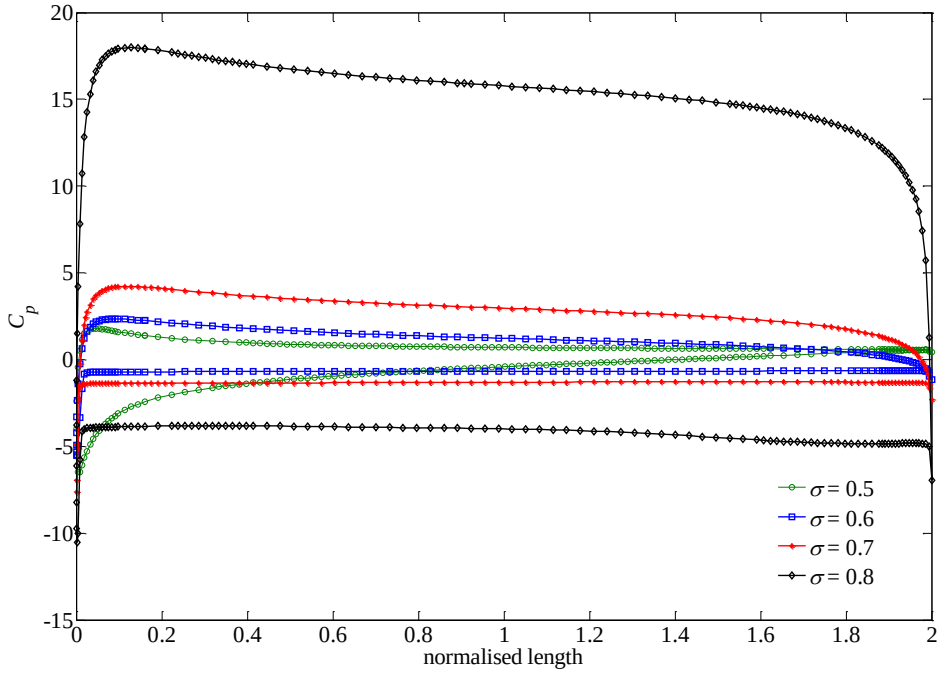

Fig. 11 Surface pressure distributions on cascade blade for different solidities at $\alpha_m = 20°$.

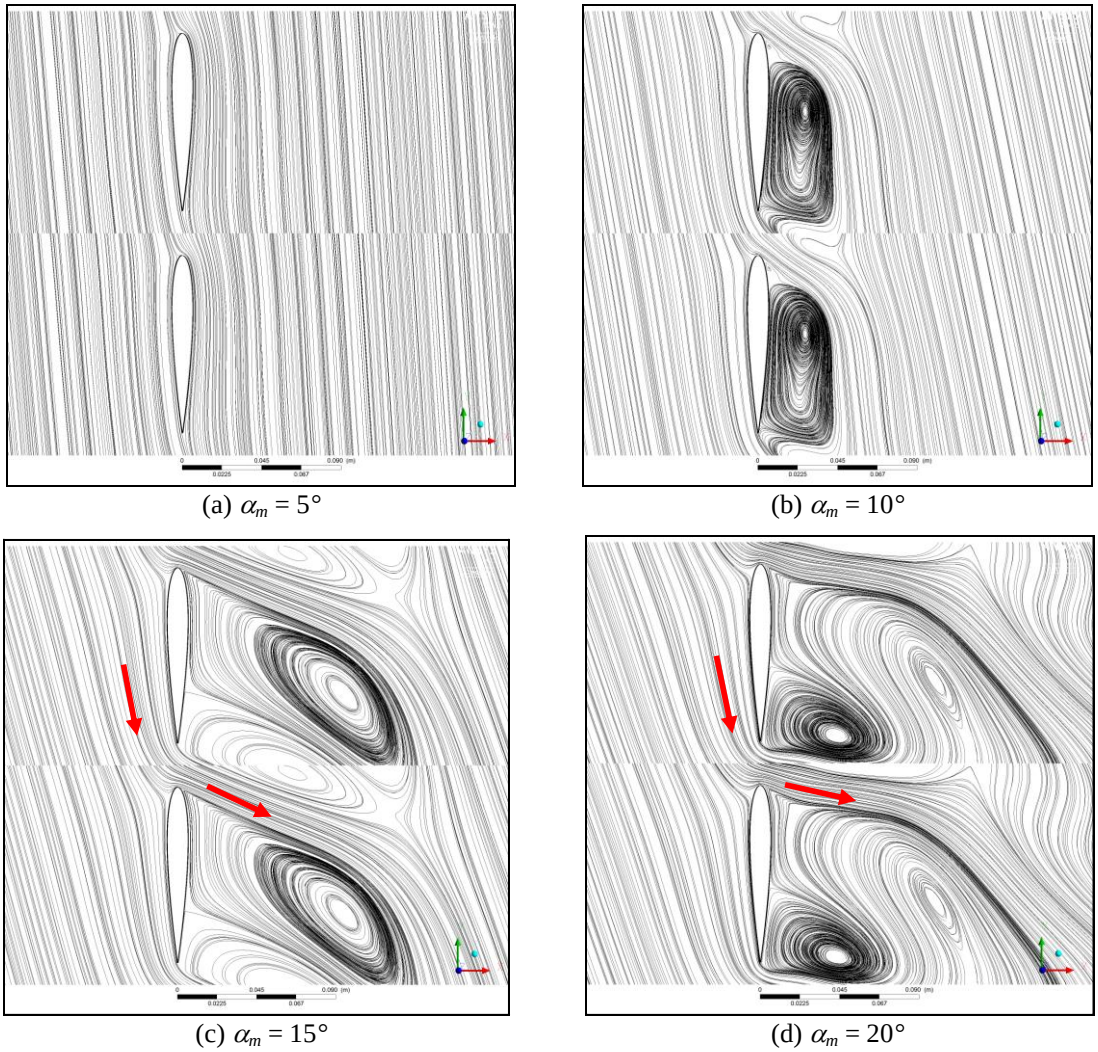

(a) $\alpha_m = 5°$ (b) $\alpha_m = 10°$

(c) $\alpha_m = 15°$ (d) $\alpha_m = 20°$

Fig. 12 Streamlines around cascade blade (NACA0012) with $\sigma = 0.8$ obtained with compresible model at different mean angles of incidence, α_m.

separation bubbles for the cascade contain paired recirculation secondary flow zones, whilst in isolated aerofoil the separation zone only contains single recirculation cell. This suggests that the mechanisms of separation zone formation in cascades and isolated aerofoils are different. We explore this issue in the following discussion.

As solidity increases, the mutual proximity of the aerofoils results in very significant increases to both the local velocity and the angle of attack at the leading edges of the aerofoils (see the bold arrows in Figs. 12c and d) in comparison to an isolated aerofoil. This is more so in higher attack angle (Figs. 12c and d) than in lower angle (Figs. 12a and b). The combined effect is thought to initiate separation to occur closer to the leading edge and to lead to larger separation zone with paired recirculation cells. A comparison with lower solidity cascade at σ < 0.5 demonstrates that at lower solidity there is a relatively small increase in velocity at the leading edge compared to the superficial flow. Analysis of the flow fields for other solidity cascades shows that starting from σ=0.7, large increase of velocity results in strong adverse pressure gradient that in turn results in separation very close to the leading edge of the aerofoil and a separation bubble over the entire suction surface and consequently greater drag and increased pressure on the pressure side that lead to greater lift. The high velocity near the leading edge (Mach > 1) as shown in Fig. 13 leads to lower leading edge pressure and overall pressure over the blade suction side. The important difference between the compressible and incompressible models appears to be on the onset of stall. Fig. 14 shows the streamlines around the blades where stall is not seen until 15^{o} angle of attack where with compressible model stall is seen at 10^{o}.

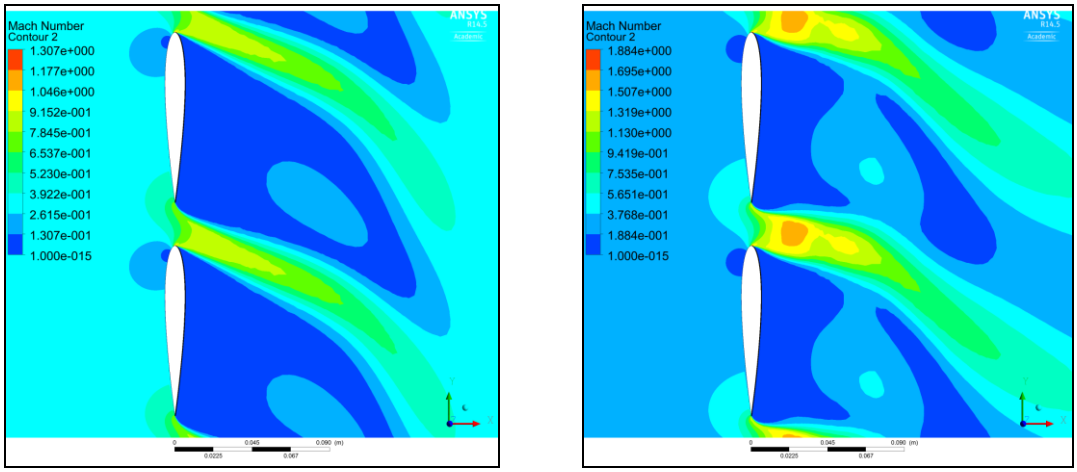

(a) α_m = 15° (b) α_m = 20°

Fig. 13 Mach number (NACA0012) in a cascade with σ = 0.8 at different mean angles of incidence, α_m .

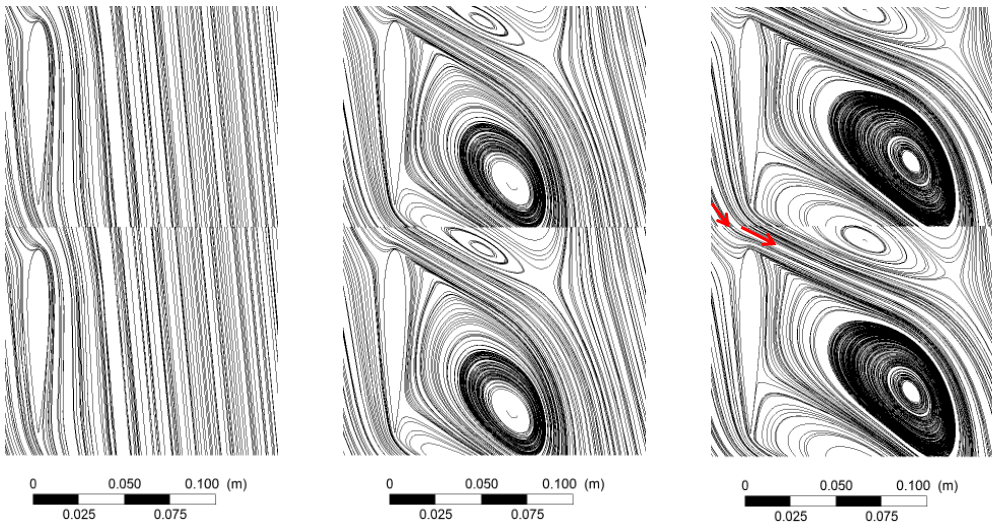

(a) α_m = 10° (b) α_m = 15° (c) α_m = 20°

Fig. 14 Streamlines around cascade blade (NACA0012) σ = 0.8 obtained with incompresible model at different mean angles of incidence, α_m.

The above analysis clearly demonstrates there is strong dependence of interference factors on solidity, stagger angle, angle of attack and compressibility. The interference between blades gives rise to high velocity in the blade spacing and greater pressure difference between the pressure and the suction sides.

5. CONCLUSIONS

Analytical lift interference factors for linear, tandem cascades (with zero stagger angle, $\gamma = 0°$) predicted by Weinig (1964) based on potential flow methods have been compared with those deduced from viscous compressible flow CFD simulations. Weinig's inviscid analysis showed that lift interference factors, k_o, for an infinite cascade is independent of the angle of attack, α, and dependent only on aerofoil stagger angle, γ, and cascade solidity, σ. Our CFD analyses have provided confirmation that Weinig's formulation, Eq. (2) is adequate for linear cascades such as NACA0012 for relatively low angles of attack ($\alpha_m < 10°$) prior to the incidence of stall.

However, at higher angles of attack ($\alpha_m > 10°$) the present analyses have shown that the interference factor, k_o, depends on both angle of attack and solidity. This is shown to be due to a number of factors including viscous and compressibility effects that result in earlier flow separation and stall for cascade compared to single aerofoil, and the influence of the finite thickness of the aerofoils, as compared to the infinitesimally thin foils assume in inviscid flow analyses. Of particular note are the effects of high cascade solidity, which increases the local flow velocity, and angle of attack at the vicinity of the leading edges of the aerofoils, leading to changes in flow separation and recirculation on the suction side of the aerofoils as compared to an isolated aerofoil.

The issues dealt with in the present work may be important in a wide range of flow situations, including blade element modelling of turbines under unsteady and/or reciprocating flow conditions. Analysis of air turbines for Oscillating Water Column Wave Energy Convertors (OWC-WECs) is a case in point, where in practice the OWC-WEC turbine aerofoils may operate under stalled conditions for significant portions of the reciprocating air flow process through the turbine. Lastly it is noted that further work is still needed to address the 3D effects due to the radial variation of the solidity.

NOMENCLATURE

c	aerofoil chord length
C_D	drag coefficient
C_L	lift coefficient
C_{L0}	lift coefficient of isolated aerofoil
C_p	pressure coefficient, $= \dfrac{p - p_r}{\frac{1}{2}\rho W^2}$
k_o	lift interference factor, $= C_L/C_{L0}$
p	pressure
p_r	reference pressure
Re	Reynolds number, $= c\,W/\nu$
s	cascade pitch
u_τ	friction velocity, $= \sqrt{\tau_w/\rho}$
V_A	axial relative velocity
V_T	tangential relative velocity
W	relative velocity
y^+	Reynolds number, $= u_\tau y/\nu$
α	angle of attack
β	angle of incidence
γ	blade stagger angle
ρ	density
ν	kinematic viscosity
σ	solidity ($= c/s$)

REFERENCES

1. Alcorn RG, Finnigan TD (2004). Control strategy development for an inverter controlled wave energy plant. *International Conference on Renewable Energy and Power Quality (ICREPQ)*, Barcelona, Spain.
2. Brito-Melo A, Neuman F, Sarmento AJNA (2008). Full-scale data assessment in OWC Pico plant. *Int. J. Offshore and Polar Engineering* 18:27-34.
3. Gareev A (2011). *Analysis of Variable Pitch Air Turbines for Oscillating Water Column (OWC) Wave Energy Converters*. Doctor of Philosophy thesis. School of Mechanical, Materials and Mechatronic Engineering, University of Wollongong, Australia. Available at: http://ro.uow.edu.au/theses/3418.
4. Gato LMC, Falcao AFD (1984). On the theory of the Wells turbine. *J. Engineering for Gas Turbines and Power* 106:628-633.
5. Gato LMC, Falcao AFD (1988). Aerodynamics of the Wells turbine. *J. Mech. Sci.* 30:383-395.
6. Govardhan M, Chauhan VS (2007). Numerical studies on performance improvement of self-rectifying air turbine for

wave energy conversion. *Engineering Applications of Computational Fluid Mechanics* 1(1):57-70.
7. Kumar KN, Govardhan M (2010). Numerical study of effect of streamwise end wall fences on secondary flow losses in two dimensional turbine rotor cascade. *Engineering Applications of Computational Fluid Mechanics* 4(4):580-592.
8. Ocean Power Technology (2012). Available at: http://www.oceanpowertechnologies.com (Accessed November 22, 2012).
9. Pelamis (2012). Available at: http://www.pelamiswave.com (Accessed November 22, 2012).
10. Raghunathan S, Setoguchi T, Kaneko K (1990). Predictions of aerodynamic performance of Wells turbines from aerofoil data. *Trans. ASME J. Turbomachinery* 112:792-795.
11. Raghunathan S (1995). The Wells air turbine for wave energy conversion. *J. Prog. Aerosp. Sci.* 31:335-386.
12. Raghunathan S (1996). Aerodynamics of cascade at a stagger angle of 90 degrees. *Proceedings of the 34th Aerospace Sci. Meeting & Exhibit.* 15-18 Jan, Reno, NV, USA, AA 96-0283.
13. Raghunathan S (1988). Aerodynamic forces on airfoils at high angles of attack, AIAA, *Proceedings of the 1st National Fluid Dynamic Congress*, Cincinnati, USA 1988.
14. Raghunathan S, Beattie WC (1996). Aerodynamic performance of contra-rotating Wells turbine for wave energy conversion. *Proceedings of IMechE* 210:421-447.
15. Sheldahl RE, Klimas P (1981). Aerodynamic characteristics of seven symmetrical airfoil sections through 180-degree angle of attack for use in aerodynamic analysis of vertical axis wind turbines. *Sandia National Laboratories Energy Report*, SAND80-2114.
16. Sun H, Li J, Feng Z (2012). Investigations on aerodynamic performance of turbine cascade at different flow conditions. *Engineering Applications of Computational Fluid Mechanics* 6(2):214-223.
17. Torresi M, Camporeale SM, Pascazio G (2009). Detailed CFD analysis of the turbine steady flow in a Wells turbine under incipient and deep stall conditions. *Journal of Fluid Engineering* 131:071103-1 – 071103-17.
18. Weinig FS (1964). Section B: Theory of two-dimensional flow through cascades. In: *Aerodynamics of turbines and compressors*. Princeton University Press, 13-81.
19. Whittaker TJT, Beattie W, Folley M, Boake C, Wright A, Osterried M, Heath T (2003). Performance of the LIMPET Wave Power Plant – prediction, measurement and potential. *Proceedings of the 5th European Wave Energy Conf.*, Cork, paper FS5.